Plasmonics (2025) 20:11299–11310
https://doi.org/10.1007/s11468-025-03185-z

RESEARCH

Ultra-sensitive D-Type PCF-SPR Biosensor with Dual-layer Au/TiO_2 Coating for Early Cancer Cell Detection

Yuan Sun[1] · Jingwei Lv[1] · Famei Wang[2] · Wei Liu[1] · Jianxin Wang[1] · Zao Yi[3] · Miao Liu[4] · Qiang Liu[1] · Paul K. Chu[5,6,7] · Chao Liu[1]

Received: 9 June 2025 / Accepted: 10 July 2025 / Published online: 23 July 2025

Abstract

A highly sensitive D-type photonic crystal fiber (PCF) sensor based on surface plasmon resonance (SPR) is proposed for the detection of cancer cells through refractive index (RI) monitoring. The sensor features a semicircular groove on the polished surface, coated with dual layers of gold (Au) and titanium dioxide (TiO_2) to enhance plasmonic coupling. Finite element method (FEM) analysis shows that the sensor has a refractive index range, maximum wavelength sensitivity, and resolution of 1.355–1.395, 54,000 nm/RIU, and 1.85×10^{-6} RIU, respectively, boding well for the early screening of cancer cells with a sensitivity in the range of 2500–24,285 nm/RIU. The compact sensor comprising a standard single-mode fiber with an outer diameter of 125 µm can be produced easily and has large application prospects in fields such as biomedical diagnosis, disease screening, and environmental detection.

Keywords Photonic crystal fiber · Surface plasmon resonance · Refractive index sensor · Wavelength sensitivity

Introduction

Surface plasmon resonance (SPR) has attracted much attention in the field of optical sensing due to its high sensitivity to changes in the refractive index (RI) of the environment [1, 2]. SPR occurs at the metal–medium interface due to collective oscillations of free electrons in the metal upon exposure to light, resulting in surface plasmon excitation (SPP) [3]. Owing to the high sensitivity, label-free detection, and fast response, SPR-based optical sensors have great potential in biomedical detection, environmental monitoring, and food safety [4–7]. However, traditional optical sensors suffer from technical bottlenecks. For instance, prism-based SPR sensors are bulky and susceptible to environmental interferences [8], while single-mode optical fiber SPR sensors exhibit poor mode coupling and low sensitivity [9], thus not being able to meet the stringent requirements of modern applications.

To overcome the above problems, photonic crystal fiber (PCF)–based SPR sensors are attractive. Compared with traditional sensors, PCF-SPR sensors can achieve high-sensitivity detection due to the flexible optical field modulation, low transmission loss, and easy coupling with the SPR effect [10–14]. Yang et al. have designed an SPR-based dual gold nanowire PCF sensor with the RI range of 1.34–1.41

✉ Chao Liu
msm-liu@126.com

1 School of Physics and Electronic Engineering, Northeast Petroleum University, Daqing 163318, China

2 Shenzhen Key Laboratory of Ultra-Intense Laser and Advanced Material Technology, Center for Intense Laser Application Technology, and College of Engineering Physics, Shenzhen Technology University, Shenzhen 518118, China

3 Joint Laboratory for Extreme Conditions Matter Properties, Southwest University of Science and Technology, Mianyang 621010, China

4 Northeast Petroleum University, Qinhuangdao Campus, Qinhuangdao 066044, China

5 Department of Physics, City University of Hong Kong, Tat Chee Avenue, Kowloon, Hong Kong, China

6 Department of Materials Science and Engineering, City University of Hong Kong, Tat Chee Avenue, Kowloon, Hong Kong, China

7 Department of Biomedical Engineering, City University of Hong Kong, Tat Chee Avenue, Kowloon, Hong Kong, China

and maximum spectral sensitivity of 46,800 nm/RIU [15]. However, the coupling efficiency and preparation process must be improved. In this respect, the D-type PCF with the unique side-polished structure allows the metal layer to be directly deposited in the neighboring region of the fiber core, thus shortening the coupling distance between the guiding mode and the SPP mode [16]. This design not only enhances the concentration of the electric field at the metal interface, which contributes to a more efficient excitation of the SPR effect, but also simplifies the fabrication process [17]. Zhang et al. have designed a D-type microchannel structure by introducing gold (Au) and molybdenum dioxide (MoO_2) as the plasmonic materials inside the microchannels with an RI detection range of between 1.33 and 1.39 and a maximum wavelength sensitivity of 17,178 nm/RIU [18]. Despite the relatively wide RI detection range, the drawbacks are low sensitivity and poor matching between the selected materials. Ashrafian et al. have proposed a D-type PCF-based SPR refractive index sensor comprising Au and titanium dioxide (TiO_2) as the plasmonic materials for the detection of cancer cells. The sensor exhibits a peak spectral sensitivity of 47,000 nm/RIU in the RI range of 1.25–1.43 [19]. However, the structure is complicated, making manufacturing difficult.

In this study, a high-sensitivity D-type PCF-SPR sensor is designed and demonstrated for the RI detection. The sensor consists of a semicircular groove on the polished side of the PCF, and the plasmonic film is deposited onto the groove to excite SPR. The distance between the fiber core and sensing layer is reduced to enhance the coupling efficiency between the guided wave mode and the surface plasmonic wave. The sensing characteristics of the sensor are systematically analyzed by the finite element method (FEM). The results show that the sensor has a refractive index detection range, maximum wavelength sensitivity, optimal resolution, and quality factor of 1.355–1.395, 54,000 nm/RIU, 1.85×10^{-6} RIU, and 86.63 RIU^{-1}, respectively. The ability of the sensor to detect a variety of cancer cells in early screening, including skin cancer, cervical cancer, blood cancer, and adrenal cancer, is investigated. The experimental results show that the sensor has enormous potential in biomedical monitoring, such as the early diagnosis of cancer.

Structure and Methodology

Figure 1a illustrates the two-dimensional cross-section of the D-type PCF sensor. The outermost layer is the perfectly matched layer (PML), which is employed to eliminate reflections at the computational boundaries and to ensure the reliability of the simulation results. In addition, a refined mesh is applied throughout the simulation to further improve computational accuracy. The analyte layer is located outside the sensor. The PCF consists of air holes of three different sizes arranged in regular rows, and the radii of the three air holes are r_1, r_2, and r_3, respectively. The air hole spacing (Λ) is the distance between the centers of two adjacent holes in the optical fiber, and r is the radius of the semicircular notch region with a D-polishing depth of H. SPR is excited by depositing a plasmonic film onto the semicircular notch. The common plasmonic metals are gold (Au), silver (Ag), and aluminum (Al). Nanomaterials such as graphene, titanium dioxide (TiO_2), or zinc oxide (ZnO) can be incorporated into the plasmonic film [20–22] to not only promote plasmonic excitation but also enhance the dielectric properties and charge transfer [23]. In particular, Au is superior due to its stable properties and oxidation resistance [24]. TiO_2 has a high refractive index, leading to strong electric field coupling between the gold layer and fiber [25]. Hence, Au and TiO_2 are selected to be the sensing materials. The Au and TiO_2 thicknesses are t_{Au} and t_{Ti}. This structure not only confines the energy in the fiber core but also controls the core size by adjusting the size and spacing of the air holes to improve the coupling strength between the fundamental mode and the SPP mode. Figure 1b shows the three-dimensional structure of the sensor. The preparation process contains the following key steps. The stacking-stretching process is adopted. The solid silicon rods and quartz capillaries are stacked in a preset arrangement and then stretched at a high temperature to form the optical fiber pre-fabricated rods with regular micrometer-sized air-hole arrays. Precise regulation of the air-hole diameters can be achieved by controlling the inner diameter size of the capillaries. One side of the fiber is processed into a D-type planar structure by precision mechanical polishing. In order to enhance SPR, a semicircular groove is etched in the D-plane by a focused ion beam (FIB) [26]. Finally, the Au thin film and TiO_2 functional layer are deposited sequentially onto the inner surface of the notch by magnetron sputtering [27].

Figure 1c shows the schematic of the sensing setup. A broadband light source transmits light through a single-mode fiber (SMF) to the D-type PCF sensing region to excite SPR. The sensor is fixed on a slide and placed on the test bench, while the analyte is placed on the sensor to make full contact. The light signal passing through the sensing region is transmitted to the optical spectrum analyzer (OSA) through the second SMF connected to the computer for real-time acquisition and analysis of the interference spectra. Afterward, it is cleaned with deionized water to eliminate residues and ensure the accuracy of the next experiment.

The effects of the structural parameters on the sensing characteristics are systematically investigated using the loss spectra. The optimal structural parameters are determined to be $r=13.5$ µm, $r_1=6$ µm, $r_2=14$ µm, $r_3=16$ µm, $\Lambda=34.5$ µm, $H=43.5$ µm, $t_{Au}=50$ nm, and $t_{Ti}=30$ nm. Fused silica is the bulk material in the sensor, and the properties are derived by the Sellmeier equation [28]:

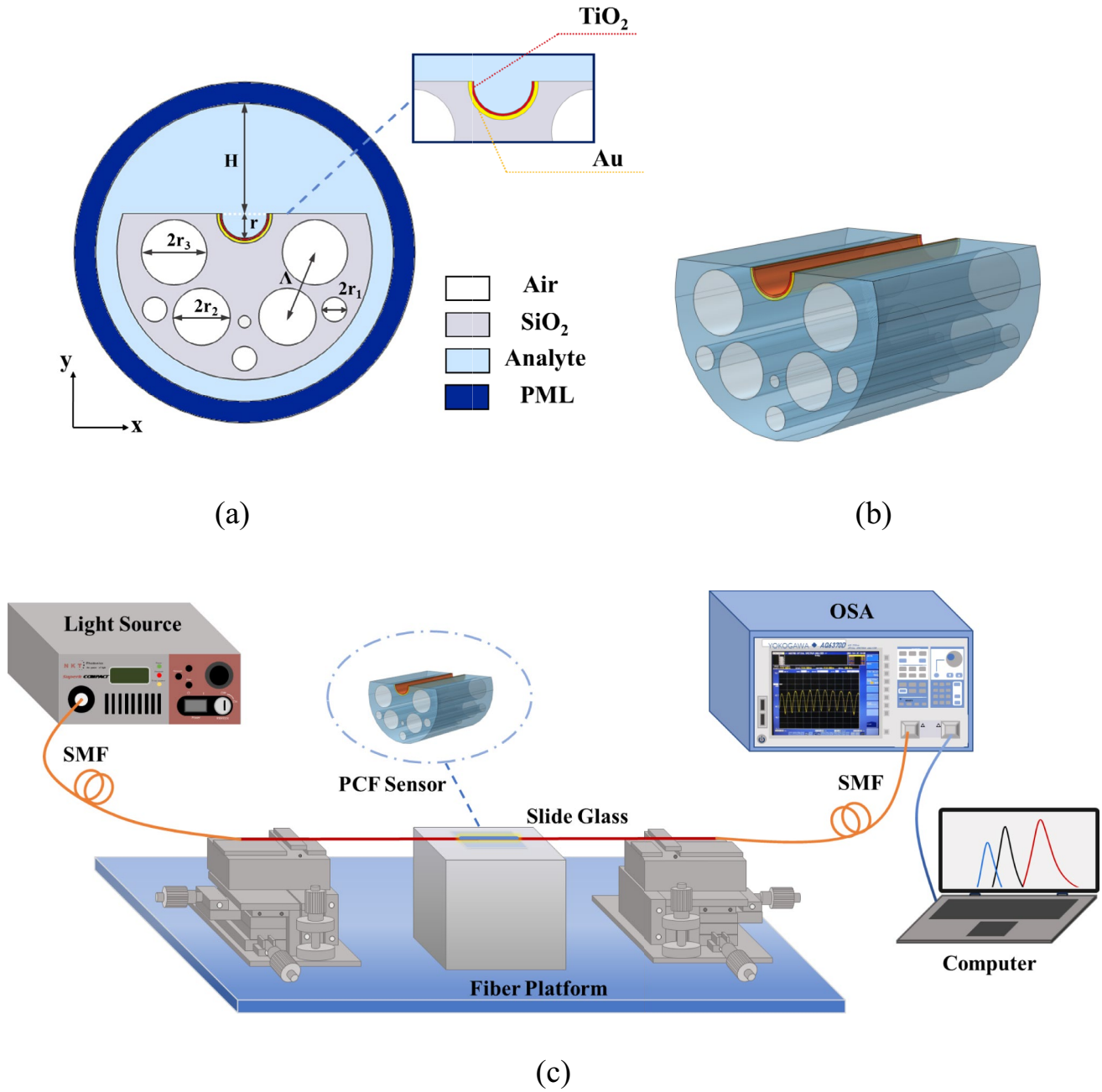

Fig. 1 **a** Schematic of the 2D cross-section of the PCF-SPR sensor; **b** schematic of the 3D structure; **c** experimental setup for practical applications

$$n_{SiO_2}(\lambda) = \sqrt{1 + \sum_{i=1}^{3} \frac{A_i \lambda^2}{\lambda^2 - B_i^2}} \tag{1}$$

where λ is the wavelength of incident light, $A_1 = 0.6961663$, $A_2 = 0.4079426$, $A_3 = 0.8974794$, $B_1 = 0.0684043$, $B_2 = 0.1162414$, and $B_3 = 9.89616$. In the designed sensor, gold is employed as the plasmonic material, and its dielectric constant is characterized using the Drude–Lorentz model [29]:

$$\varepsilon_{Au} = \varepsilon_{\infty} - \frac{\omega_D^2}{\omega(\omega + j\gamma_D)} - \frac{\Delta_\varepsilon \Omega_L^2}{(\omega^2 - \Omega_L^2) + j\Gamma_L \omega} \tag{2}$$

where the dielectric constant $\varepsilon_\infty = 5.9673$, weighting factor $\Delta_\varepsilon = 1.09$, incident angular frequency $\omega = 2\pi c/\lambda$,

plasma frequency $\omega_D = 4227.2\pi$ (THz), damping frequency $\gamma_D = 31.84\pi$ (THz), Lorentz oscillator frequency $\Omega_L = 1300.14\pi$ (THz), and Lorentz oscillator spectral width $\Gamma_L = 209.72\pi$ (THz).

In order to enhance the coupling strength between the fiber core guiding mode and the surface plasmonic mode, a thin nano-TiO_2 film is introduced to the gold surface. The refractive index of TiO_2 can be calculated by the following equation [19]:

$$n_{TiO_2} = \sqrt{5.193 + \frac{2.441 \times 10^7}{\lambda^2 - 0.803 \times 10^7}} \tag{3}$$

In general, the imaginary part of the effective refractive index ($\mathrm{Im}(n_{eff})$) is associated with the transmission loss of the mode. By calculating the resonance peak shift in the loss spectrum, the sensitivity and other performance characteristics of the sensor can be determined. The limiting loss (CL) reflects the degree of radiation or absorption loss of energy during SPR and can be calculated by the following equation [30]:

$$\alpha_c = \frac{20}{\ln 10}\frac{2\pi}{\lambda}\mathrm{Im}(n_{eff}) = 8.686 \times \frac{2\pi f}{c}\mathrm{Im}(n_{eff}) \times 10^4 \tag{4}$$

where λ is the incident light wavelength and $\mathrm{Im}(n_{eff})$ is the imaginary part of the effective refractive index of the fiber base mode. Optical biosensors typically employ wavelength detection to monitor and analyze biomolecular interactions. This method tracks resonance wavelength shifts induced by refractive index changes near the sensor surface. Spectral sensitivity, also known as wavelength sensitivity (WS), is a key parameter for evaluating the performance of PCF-SPR sensors and can be calculated from the resonance wavelength shift using the following equation [31]:

$$S_\lambda(\mathrm{nm/RIU}) = \frac{\Delta\lambda_{peak}}{\Delta n_a} \tag{5}$$

where $\Delta\lambda_{peak}$ is the distance in wavelength between the two peaks and Δn_a is the change in RI of the analyte. The figure-of-merit (FOM) is defined as the ratio of wavelength sensitivity to the full width at half maximum (FWHM). A higher FOM indicates greater detection accuracy. FOM is defined as follows [32]:

$$\mathrm{FOM} = \frac{S_\lambda}{\mathrm{FWHM}} \tag{6}$$

where S_λ is the wavelength sensitivity and FWHM is the full-width at half-maximum of the resonant loss spectrum when the curve reaches half of the maximum loss. To further evaluate the ability to detect small changes in the refractive index, a performance parameter of resolution is introduced and defined as [33]

$$R(\mathrm{RIU}) = \Delta n_a \times \frac{\Delta\lambda_{\min}}{\Delta\lambda_{peak}} \tag{7}$$

where Δn_a is the refractive index change, $\Delta\lambda_{\min}$ is the minimum resolution of the spectrometer, and $\Delta\lambda_{peak}$ is the maximum displacement of the plasma resonance wavelength. Amplitude sensitivity (AS) is also a key parameter for evaluating the performance of refractive index sensors and is commonly used to quantify the magnitude of loss variation induced by a unit change in refractive index. It is calculated as follows:

$$S_A(\mathrm{RIU}^{-1}) = \frac{\Delta\alpha_{loss}}{\Delta n_a \times \alpha_{neff}} \tag{8}$$

where α_{neff} represents the loss amplitude and $\Delta\alpha_{loss}$ denotes the peak change in loss between two consecutive refractive indices. In addition to sensitivity, the signal-to-noise ratio (SNR) and detection accuracy (DA) further reflect the sensor's detection stability and resolution, and they are calculated as follows:

$$\mathrm{SNR} = \frac{\Delta\lambda_{peak}}{\mathrm{FWHM}} \tag{9}$$

$$\mathrm{DA} = \frac{1}{\mathrm{FWHM}} \tag{10}$$

These parameters are crucial for evaluating the sensing performance and feasibility of the sensor and offer a theoretical foundation for its further optimization in future research.

Analysis

Figure 2 illustrates the dispersion relations of the SPP mode, fundamental mode, and confinement loss with wavelength. The black curve in the figure represents the variation of fundamental mode loss with wavelength for the y-polarized state. The loss increases gradually with wavelength, reaching the maximum at the resonant wavelength. The loss tends to decrease with further increase in the wavelength. The red and blue lines in the figure indicate the real part of the effective refractive index of the fundamental mode and SPP mode, respectively. As the wavelength increases gradually, the effective RI real part of the two modes decreases at different rates and intersects at 2590 nm, and the wavelength corresponding to the intersection point is equal to the wavelength corresponding to the loss peak. This indicates that the two modes satisfy the phase matching condition for SPR. Illustrations a and b show the E-field distributions of the fundamental and SPP modes, respectively, when the sensor is non-resonant, and illustration c shows the E-field distribution of the fundamental mode at resonance. The three

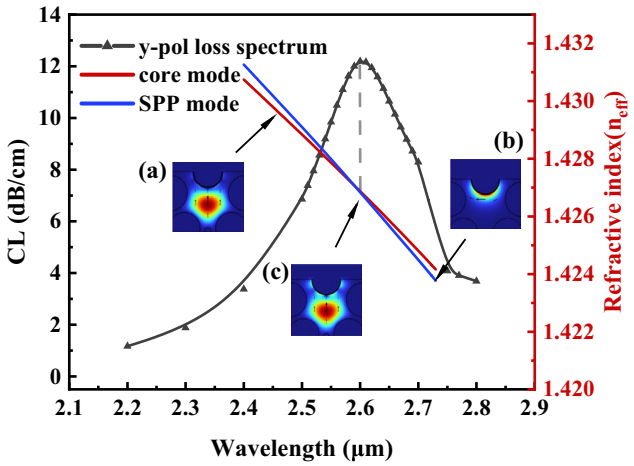

Fig. 2 Dispersion curves of the SPP mode (blue) and core-guided mode (red) and the wavelength-dependent confinement loss (black), at RI = 1.36

electric field plots show that for non-resonance, the energy is mainly concentrated within the fiber core. When resonance occurs, the energy in the core is maximally coupled to the surface of the sensing layer consisting of Au and TiO_2 films to produce a loss peak. The relationship curves and electric field distributions express the basic principle and significance of SPR.

Figure 3 demonstrates the effects of different stomatal parameters on the loss spectra. Figure 3a shows that the resonant wavelength redshifts as the stomatal spacing (Λ) increases from 32.5 to 36.5 μm (in steps of 2 μm) because a larger Λ widens the distance between the air holes, weakens the binding ability of the optical field inside the core, increases the energy leakage outward, and increases the phase velocity of the incident light in the core. Hence, the wavelength corresponding to the resonance condition becomes longer. As shown in Fig. 3b, the resonance wavelength blueshifts as the radius of the macropores (r_3) increases from 14 to 18 μm (in steps of 2 μm). As r_3 increases, the air holes occupy more space, causing the

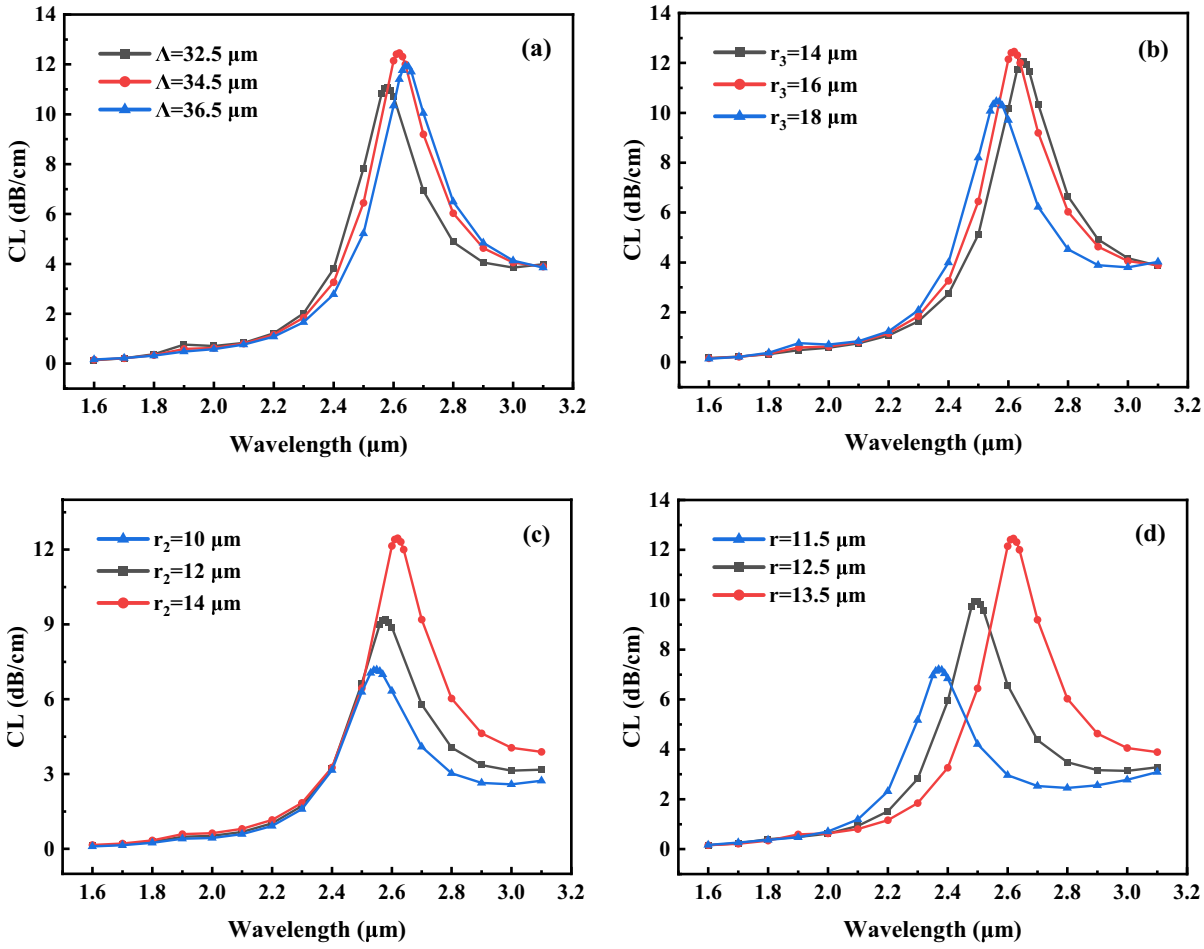

Fig. 3 Effects of air pore parameters on the loss spectra of the PCF-SPR sensor for RI = 1.36: **a** loss spectra for different air-hole spacing Λ, **b** loss spectra for different large air-hole r_3, **c** loss spectra for different medium-sized air-hole r_2, and **d** loss spectra for different notch-polishing r

optical field to further concentrate in the core region. More energy is bound to the core with a high refractive index, resulting in a decrease in the phase velocity of the incident light in the core. Consequently, the wavelength corresponding to the resonance condition becomes shorter. Figure 3a and b show that the changes of Λ and r_3 have little effect on the loss peaks, indicating that the modulation of the loss spectrum by the air-hole spacing and large air-hole radius is limited. Figure 3c shows that as the medium-sized stomatal radius (r_2) increases from 10 to 14 μm (in steps of 2 μm), the loss peak increases with r_2. This phenomenon occurs because the fiber core is squeezed by the enlarged medium-sized air holes, and more energy is coupled to the metal nanolayer notches to enhance SPR coupling and increase the loss. As shown in Fig. 3d, the peak loss increases gradually as the radius (r) of the semicircular notch increases from 11.5 to 13.5 μm (in steps of 1 μm) because the larger notch increases the contact area between the metal nanolayer and the fiber core mode. Based on the above single-variable simulation analyses of the air-hole pitch, large air-hole radius, medium air-hole radius, and the semi-circular groove radius, the influence trends of each structural parameter on the resonance wavelength and loss peak were determined. To ensure high sensitivity, a distinct resonance peak, and good fabrication feasibility, the following structural parameters were selected as the optimal configuration: $r = 13.5$ μm, $r_2 = 14$ μm, $r_3 = 16$ μm, and $\Lambda = 34.5$ μm.

Figure 4 illustrates the effect of polishing depth (H) on the loss spectra of the PCF-SPR sensor. As H increases from 39.5 to 43.5 μm (in steps of 2 μm), there is almost no effect on the resonance wavelength, but the loss peak increases with H. The effect of polishing depth is similar to that caused by deepening the notch. That is, the coupling distance between the metal nanolayer and the fiber core decreases. This is similar to the effect arising from increasing the notch depth. The coupling distance between the metal nanolayer and the fiber core decreases to enhance the coupling strength and SPR, leading to a rise in the loss peak due to more efficient coupling of energy from the fundamental mode to the surface plasma wave.

Figure 5a shows the effects of different TiO_2 film layer thicknesses. A thicker TiO_2 film produces a blueshift of the resonance wavelength and a smaller loss peak for a fixed RI. When the TiO_2 is too thick, the ability of the optical field to penetrate the Au layer is compromised, thus reducing the efficiency of the Au layer to excite SPR. The wavelength sensitivities for different TiO_2 thicknesses of 30, 40, and 50 nm are 7000, 4000, and 5000 nm/RIU, respectively. Although the sensitivity is slightly improved for the 50-nm thickness compared to 40 nm, the loss is small, and the SPR effect is limited. Taking into account the peak loss and sensitivity, the optimal TiO_2 thickness is 30 nm.

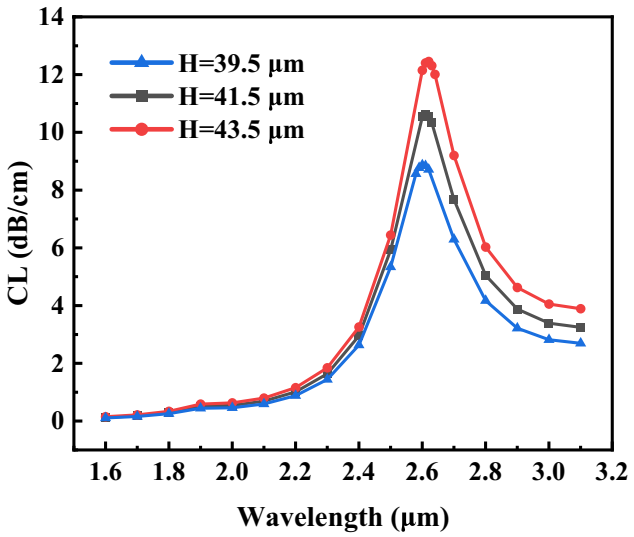

Fig. 4 Effects of the downthrow depths on the loss spectra for RI = 1.36

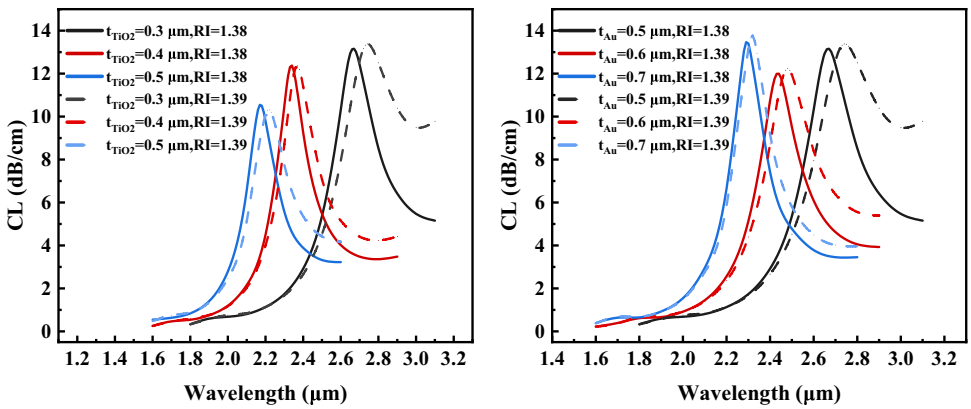

Fig. 5 **a** Loss spectra for different Au layers and **b** loss spectra for different TiO_2 layers for RI = 1.38 and 1.39

Figure 5b shows the effects of different Au layer thicknesses. The resonance peaks move to shorter wavelengths with increasing Au layer thickness for a fixed RI. If the Au film is too thick, the incident electromagnetic wave cannot penetrate deeply inside the metal, and the electric field cannot reach the interface between the metal and dielectric to hamper SPP excitation. Since SPR depends on the strong coupling between the guided wave mode and SPP, resonance becomes insignificant in this case, and the coupling efficiency decreases significantly. Further assessment of the wavelength sensitivities for different Au thicknesses shows that the wavelength sensitivities are 7000, 4000, and 3000 nm/RIU when the Au thicknesses are 50, 60, and 70 nm, respectively. The optimal Au layer thickness is 50 nm.

The loss spectra are simulated for the RI range of 1.355–1.395 (with an increment of 0.005), as shown in Fig. 6. It can be clearly observed that within the operating wavelength range of 2 to 3 μm, the resonance wavelength gradually redshifts as the RI increases. This wavelength band exhibits favorable molecular absorption characteristics, making it suitable for high-sensitivity detection. Figure 6a shows a peak wavelength of 2610 nm for an RI of 1.355 and the smallest loss peak. In comparison, the loss peak is the largest, and the peak wavelength reaches 3010 nm at an RI of 1.395, indicating that the coupling between the fundamental mode and the SPP mode is the strongest. When the RI exceeds 1.395, the confinement of the guided mode weakens, resulting in optical field leakage, reduced sensitivity, and irregular resonance peaks. In contrast, when the RI falls below 1.355, the coupling between the fundamental mode and the SPP mode becomes insufficient, leading to poor sensing performance and low detection accuracy. Therefore, the RI range of 1.355 to 1.395 is considered the optimal sensing interval for this sensor. Figure 6b shows that the peak wavelength shifts from 2710 to 3010 nm when the RI changes from 1.39 to 1.395, showing a maximum shift of 300 nm. According to Eq. 5, the maximum sensitivity is 54,000 nm/RIU.

Discussion

The histograms of the wavelength sensitivity for different RIs are displayed in Fig. 7a. The wavelength sensitivity increases gradually from 2000 nm/RIU. The maximum spectral sensitivity is 54,000 nm/RIU, and the average sensitivity is 11,142 nm/RIU. Figure 7b shows the polynomial fit of the resonance wavelengths with RI with an *R*-square of 0.98406.

In order to provide a more comprehensive analysis of the sensor performance, AS, SNR, and DA are further introduced as auxiliary evaluation parameters in this study. Figure 8a illustrates the variation of amplitude sensitivity with wavelength as the RI changes from 1.380 to 1.395, with a step size of 0.005. In biosensor applications, amplitude sensitivity reflects the sensor's ability to detect changes in signal amplitude caused by variations in analyte concentration or specific biomolecular interactions. It can be observed that as the RI increases, the AS generally exhibits a gradual decreasing trend and shows a consistent response pattern across the wavelength range, accompanied by a slight redshift. Figure 8b and c present the changes in SNR and DA within the RI range of 1.355–1.395. As shown in Fig. 8b, the SNR increases with RI and reaches 0.44 at an RI of 1.395, indicating good detection stability and reliable signal response. Figure 8c demonstrates that the DA decreases with increasing RI, which is consistent with expected behavior, suggesting that the sensor maintains relatively stable resolution capabilities for small refractive index variations within the sensing range.

The effects of different metal oxide layers are studied in order to select the optimal metals, including molybdenum

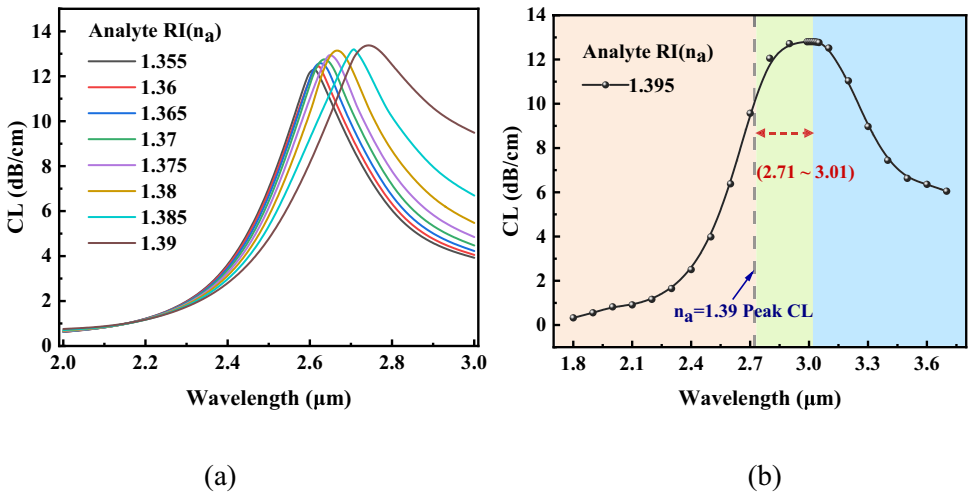

Fig. 6 Loss spectra: **a** RI between 1.355 and 1.39 and **b** RI of 1.395

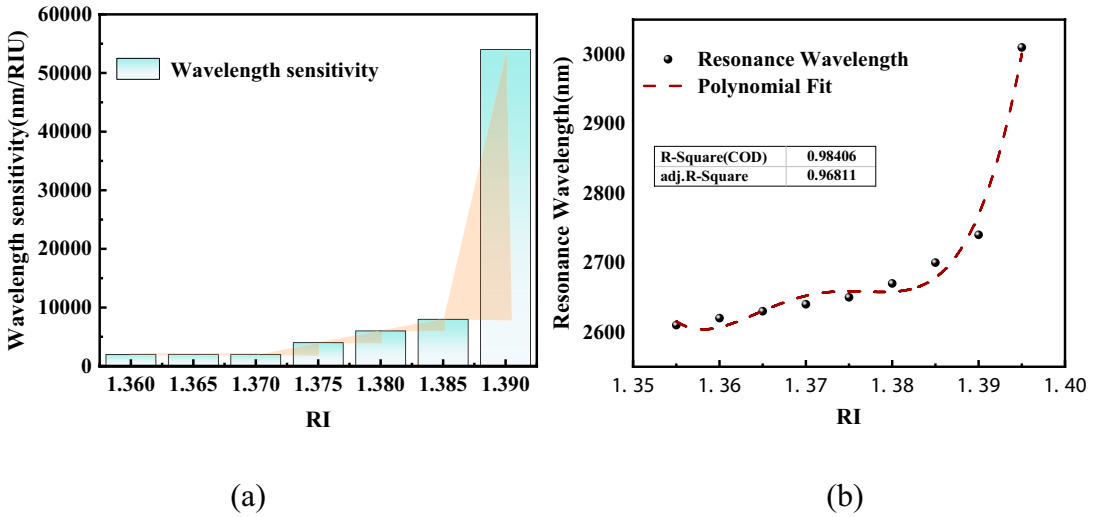

Fig. 7 **a** Dependence of sensitivity on analyte RI and **b** polynomial fit of resonant wavelengths

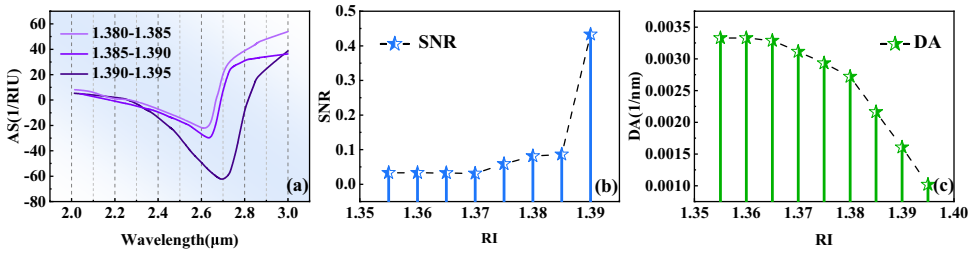

Fig. 8 Properties of the PCF-SPR sensor: **a** AS, **b** SNR, and **c** DA

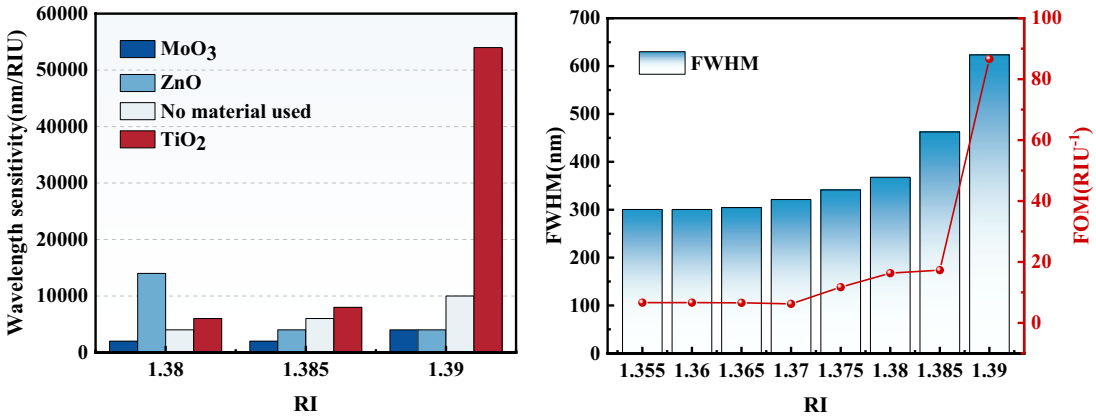

Fig. 9 **a** Effects of different metal oxides on the wavelength sensitivity, **b** full-width at half-maximum (FWHM) and figure-of-merit (FOM) of the sensor

trioxide (MoO_3), ZnO, and TiO_2. Figure 9a shows the wavelength sensitivity in the RI range of 1.38–1.39 (in steps of 0.005). The effects of different materials on the SPR coupling efficiency vary significantly. The sensitivities of the uncoated group are 4000, 6000, and 10,000 nm/RIU, respectively. The sensitivity of MoO_3 is lower than that of the control group for all RIs, indicating that its small low refractive index cannot excite SPP efficiently and even inhibits

Table 1 Properties of the sensors for refractive indexes between 1.355 and 1.395

RI of analyte	λ_{peak} (nm)	Resolution (RIU)	Wavelength sensitivity (nm/RIU)	FOM (RIU^{-1})
1.355	2610	5.0×10^{-5}	2000	6.65
1.36	2620	5.0×10^{-5}	2000	6.66
1.365	2630	5.0×10^{-5}	2000	6.57
1.37	2640	5.0×10^{-5}	2000	6.22
1.375	2650	5.0×10^{-5}	4000	11.72
1.38	2670	2.5×10^{-5}	6000	16.31
1.385	2700	1.67×10^{-5}	8000	17.30
1.39	2740	1.25×10^{-5}	54,000	86.63
1.395	3010	1.85×10^{-6}	N/A	N/A

SPR generation. In contrast, ZnO shows a higher sensitivity for RI = 1.38 (up to 14,000 nm/RIU), but the sensitivity decreases rapidly at higher RIs. Hence, it is more sensitive to the modulation effect of the electromagnetic field distribution and has poor coupling stability. TiO_2 shows the best enhancement, as its high refractive index leads to a stronger electric field compression effect at the metal–dielectric interface and enhances the coupling strength between the guided-wave mode and the SPP mode. The structure exhibits enhanced sensitivity for all RIs up to 540,000 nm/RIU, thereby corroborating that TiO_2 is the best material. The regulation mechanism of SPR for different metal oxides mainly stems from their refractive index properties, electric field distribution regulation ability, and the interfacial coupling strength. On account of the high refractive index and good optical transmission properties, TiO_2 shows strong for a wide RI range.

Figure 9b shows the FWHM and FOM for different refractive indexes. They increase slowly and then increase significantly in this RI range. The resonance wavelength (λ_{peak}), resolution, wavelength sensitivity, and FOM are summarized in Table 1. Each parameter shows an increasing trend as the RI increases from 1.355 to 1.395. The offset of the resonance wavelength increases continuously to improve the wavelength sensitivity. The structure achieves the optimal resolution (1.85×10^{-6} RIU) and FOM (86.63 RIU^{-1}) at a refractive index of 1.395. Further analysis shows that the PCF-SPR sensor has excellent sensing response under different RI conditions.

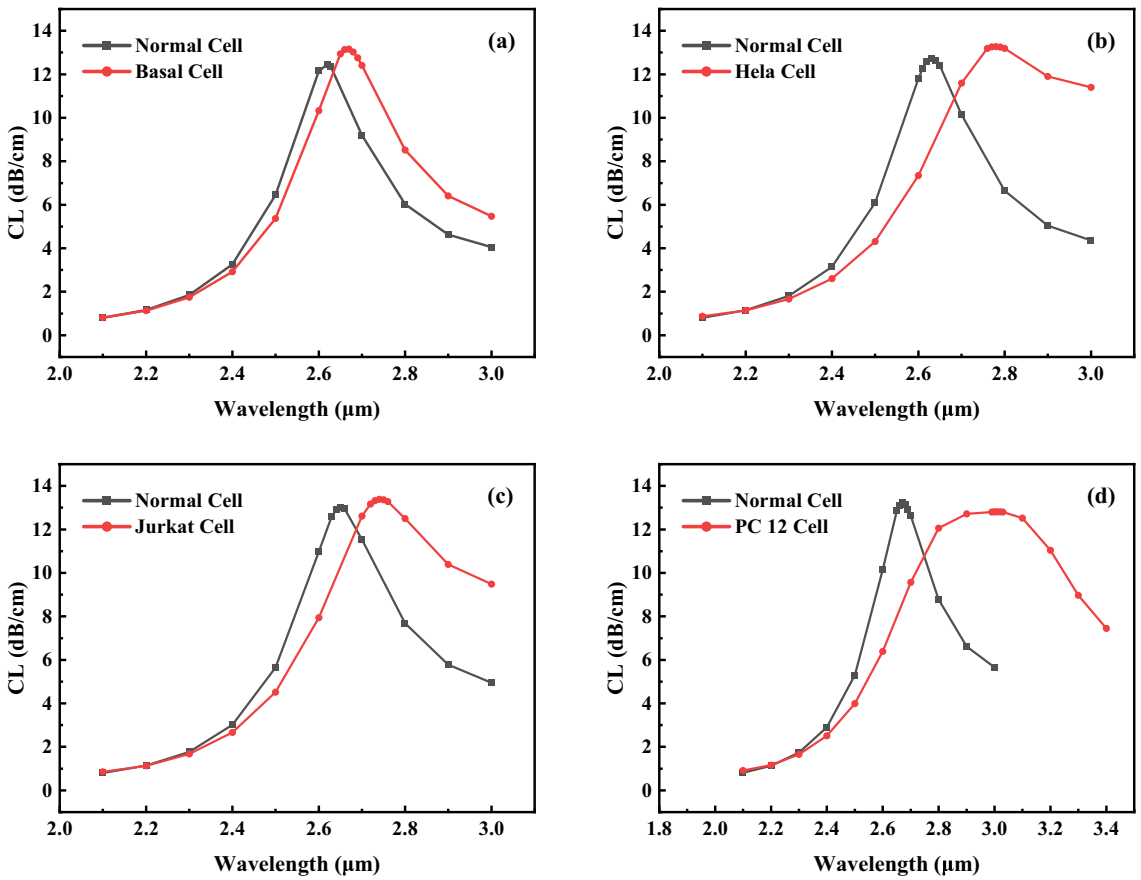

Fig. 10 Resonance wavelengths of normal and cancerous cells and limiting losses: **a** skin, **b** cervical, **c** blood, and **d** adrenal cancer

Table 2 Refractive indexes of normal and cancerous cells

Cancer cell	Cell type	Normal cell RI	Cancerous cell RI	Wavelength sensitivity (nm/RIU)	Ref
Skin	Basal	1.360	1.380	2500	[34]
Cervical	Hela	1.368	1.392	6250	[34]
Blood	Jurkat	1.376	1.390	6428	[32]
Adrenal gland	PC12	1.381	1.395	24,285	[32]

Early cancer detection relies on the difference in the refractive index of normal cells and cancer cells in the lesion state. Figure 10 shows the resonance wavelengths and limiting losses of four types of human normal cells and cancer cells. The black curve corresponds to normal cells, while the red curve represents cancer cells. The limiting loss of cancer cells is higher than that of normal cells, manifested by a redshift of the resonance peak. Notably, the confinement loss of the PC12 cancerous cell with a refractive index of 1.395 is lower than that of the corresponding normal human cell. This is because the core mode confinement weakens at this refractive index, causing a significant portion of the optical field to leak into the external analyte region. As a result, the coupling efficiency between the core mode and the SPP mode decreases, leading to a reduction in confinement loss. In order to analyze the response of various types of cells, the refractive indexes of the four normal cells and cancer cells are summarized in Table 2, which is used to analyze the loss spectra in Fig. 10. The normal cells have RIs of 1.360, 1.368, 1.376, and 1.381, and their resonance wavelengths are 2620, 2630, 2650, and 2670 nm, respectively. In contrast, Hela shows an RI of 1.392, Jurkat an RI of 1.390, and PC12 an RI of 1.395. The resonance wavelengths are 2620, 2630, 2650, and 2670 nm, respectively. PC12 shows resonance wavelengths of 2670, 2780, 2740, and 3010 nm, respectively. By analyzing the

Table 3 Comparison of different sensors

Ref.	RI range	Plasmonic Materials	Wavelength Sensitivity (nm/RIU)	Resolution (RIU)	Structure Diagram
[35]	1.33-1.38	Au	8000	1.25×10^{-5}	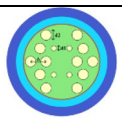
[36]	1.20-1.30	Au	10200	9.8×10^{-6}	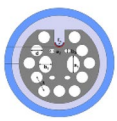
[20]	1.31-1.35	Au	20000	6.66×10^{-6}	
[37]	1.37-1.41	Ag	11700	8.55×10^{-6}	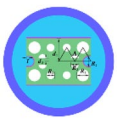
This work	1.355-1.395	Au	54000	1.85×10^{-6}	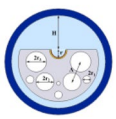

resonance wavelength shift and RI change, the wavelength sensitivities are calculated to be 2500, 6250, 6428, and 24,285 nm/RIU, respectively. The results indicate that the sensor has excellent properties in monitoring cancer cells (RI range of 1.355–1.395) for skin, cervical, blood, and adrenal cancer.

Table 3 compares different sensors. Our sensor shows a high sensitivity, a wide refractive index detection range, and a resolution of 10^{-6}. The overall performance is comparable to that of current high-precision sensors. All in all, the structure has good manufacturability, cost-effectiveness, and outstanding sensing properties suitable for clinical implementation.

Conclusion

A D-type PCF refractive index sensor based on SPR is designed and demonstrated. The sensor features a compact structure based on a standard single-mode fiber with a diameter of 125 µm and is easy to fabricate. Through structural optimization, the final optimal parameters are determined as follows: microchannel radius $r = 13.5$ µm; air-hole radii $r_1 = 6$ µm, $r_2 = 14$ µm, $r_3 = 16$ µm; air hole pitch $\Lambda = 34.5$ µm; and polishing depth $H = 43.5$ µm. To enhance the sensor's sensitivity, a 50-nm Au layer and a 30-nm titanium dioxide TiO_2 layer are deposited within the semicircular groove. Finite element analysis shows that the sensor exhibits excellent response in the analyte refractive index range of 1.355–1.395, a maximum wavelength sensitivity of 54,000 nm/RIU, a resolution of 1.85×10^{-6} RIU, and good linearity in the wide RI range. The sensor is used for the early detection of cancer cells. It can differentiate typical cancer cells such as Basal, Hela, Jurkat, and PC12. The wavelength sensitivity range of 2500–24,285 nm/RIU demonstrates the excellent ability to respond to small refractive index changes. Owing to the high sensitivity, manufacturing compatibility, and adaptability, the sensor has large potential in optical fiber biosensors for early cancer screening, disease diagnosis, and detection of complex substances.

Author Contributions Yuan Sun: Conceptualization, Methodology, Software, Writing-Original Draft. Jingwei Lv: Investigation, Validation. Famei Wang: Conceptualization, Writing- Reviewing and Editing. Wei Liu: Formal analysis. Jianxin Wang: Funding acquisition, Validation. Zao Yi: Investigation. Miao Liu: Conceptualization. Qiang Liu: Resources. Paul K. Chu: Project administration. Chao Liu: Resources, Writing- Reviewing and Editing.

Funding The work was jointly supported by the Heilongjiang Provincial Natural Science Foundation of China [JQ2023F001], National Natural Science Foundation of China [12304480], Natural Science Foundation of Heilongjiang Province [LH2021F007], China Postdoctoral Science Foundation funded project [2020M670881], as well as City University of Hong Kong Donation Research Grants [DON-RMG 9229021 and 9220061].

Data Availability No datasets were generated or analysed during the current study.

Declarations

Competing interests The authors declare no competing interests.

References

1. Ran C, Zhang J, He X et al (2024) Recent development of gold nanochips in biosensing and biodiagnosis sensibilization strategies in vitro based on SPR, SERS and FRET optical properties. Talanta 282:126936. https://doi.org/10.1016/j.talanta.2024.126936
2. Duan Q, Liu Y, Chang S et al (2021) Surface plasmonic sensors: sensing mechanism and recent applications. Sensors 21(16):5262
3. Wei Y, Zeng N, Yang Y et al (2024) Unveiling the influence of line shape of surface plasmon resonances on exciton–plasmon strong coupling. Adv Opt Mater 12(25):2400639
4. Mousavi SM, Hashemi SA, Kalashgrani MY et al (2022) Biomedical applications of an ultra-sensitive surface plasmon resonance biosensor based on smart MXene quantum dots (SMQDs). Biosensors 12(9):743
5. Das A, Huraiya MA, Tabata H et al (2024) Ultra-sensitive refractive index detection with gold-coated PCF-based SPR sensor. Talanta 10:100384
6. Ansari MTI, Raghuwanshi SK, Kumar S (2023) Recent advancement in fiber-optic-based SPR biosensor for food adulteration detection—a review. IEEE Trans NanoBiosci 22(4):978–988
7. Ahamed S, Venkatesan KK, Jalaludeen SA (2025) A review on various surface plasmon resonance-based sensors. Plasmonics. https://doi.org/10.1007/s11468-025-02837-4
8. Vasimalla Y, Pradhan HS (2022) Modeling of a novel SCHOTT B270 prism based SPR sensor using Ag-Si-BP/MXene structure for detection of specific biological samples. Opt Quantum Electron 54(10):612
9. Wei Y, Liu C, Liu C et al (2022) Single-mode fiber curvature sensor based on SPR. Appl Opt 61(15):4620–4626
10. Guedri-Knani L, Kaziz S, Dridi C (2025) Performance prediction of a highly sensitive optimized PCF-SPR biosensor for cancer cell detection using MLP-based ANN model. IEEE Sens J 25(10):17136–17143
11. Zhang Z, Yin Z, Li S (2024) A SPR sensor with wide RI measuring range and narrow FWHM based on PCF-silver film structure. J Lightwave Technol 42(20):7398–7404
12. Wang J, Lu X, Mi C et al (2024) Ultra-high sensitivity photonic crystal fiber sensor based on dispersion turning point sensitization of surface plasmonic polariton modes for low RI liquid detection. Opt Express 32(19):32895–32908
13. Yao S, Yu Y, Qin S et al (2022) Research on optimization of magnetic field sensing characteristics of PCF sensor based on SPR. Opt Express 30(10):16405–16418
14. Liu C, Wang J, Lv J et al (2025) Economical and easily implemented Vernier effect bubble microcavity FPI for strain sensing with extreme low-temperature cross-sensitivity. Infrared Phys Technol 150:105939
15. Yang X, Hou S, Xie C et al (2024) High-performance photonic crystal fiber biosensor based on surface plasmon resonance for early cancer detection. Plasmonics 19(2):675–685

16. Ifaz Ahmad Isti M, Hussayeen Khan Anik M, Nuzhat S et al (2022) Highly sensitive double D-shaped channel photonic crystal fiber based plasmonic refractive index sensor. Opt Continuum 1(3):575–590
17. Anik MHK, Isti MIA, Islam SMR et al (2020) Milled microchannel-assisted open D-channel photonic crystal fiber plasmonic biosensor. IEEE Access 9:2924–2933
18. Zhang S, Yang Y, Dong J (2024) Ultra-wide measurement range D-shaped photonic crystal fiber sensor based on surface plasmon resonance. Eur Phys J D 78(8):111
19. Ashrafian M, Olyaee S, Seifouri M (2025) Highly sensitive cancer detection using an open D-channel PCF-based SPR biosensor. Sci Rep 15(1):10168
20. Divya J, Selvendran S (2025) Performance evaluation of D-shaped photonic crystal fiber based SPR sensors with different plasmonic materials: a comparative analysis. Results Eng 26:104715
21. Rahayu TOC, Septiani NLW, Gumilar G et al (2021) Modification of gold substrate with Fe3O4-graphene nanocomposite to increase resolution of surface plasmon resonance (SPR) glucose sensor. IEEE Sens J 1(18):19959–19966
22. Yanan W, Fei Z, Meng Z et al (2023) Dependence relationship between doping modes and surface plasmon resonance properties of doped ZnO nanocrystals. Colloids Surf A 676:132103
23. Fendi FWS, Mukhtar WM, Abdullah M (2023) Surface plasmon resonance sensor for COVID-19 detection: a review on plasmonic materials. Sens Actuators A 362:114617
24. Isti MIA, Talukder H, Islam SMR et al (2020) Asymmetrical D-channel photonic crystal fiber-based plasmonic sensor using the wavelength interrogation and lower birefringence peak method. Results Phys 19:103372
25. Kouhi M (2025) Simulation of a surface plasmon resonance biosensor using a combination of TiO2 and 2D materials for blood glucose detection. Plasmonics 1–12. https://doi.org/10.1007/s11468-025-02869-w
26. Barman S, Bhattacharjee S (2024) Electric field driven focusing and transport of plasma ion beams by micro-glass capillaries beyond the self-focusing limit. J Phys D: Appl Phys 57(40):405206
27. Yang Z, Chen J, Long X et al (2024) Sensitive and repeatable optical fiber hydrogen sensors using plasma-induced oxygen vacancies magnetron sputtering coating technique. J Lightwave Technol 43(5):2428–2437
28. Manickam P, Senthil R, Senthil R (2024) Numerical analysis of hybrid-SPR-PCF multi-analyte sensor for clinical diagnosis. Plasmonics 20(6):3305–3311. https://doi.org/10.1007/s11468-024-02486-z
29. Luo B, An M, Hu T et al (2024) Dual-channel surface plasmon sensor based on photonic crystal fiber for low refractive index detection. Opt Quantum Electron 56(6):1059
30. Trisha IJ, Patwary AK, Sayem MA et al (2024) Numerical analysis of a single channel exposed core elliptical shaped PCF based highly sensitive SPR sensor for wide RI sensing. Opt Express 32(14):25472–25487
31. Wu T, Shao Y, Wang Y et al (2017) Surface plasmon resonance biosensor based on gold-coated side-polished hexagonal structure photonic crystal fiber. Opt Express 25(17):20313–20322
32. Sardar MR, Faisal M (2024) Dual-core dual-polished PCF-SPR sensor for cancer cell detection. IEEE Sens J 24(7):9843–9854
33. Chen LQ, Wu YC, Liu Y et al (2024) Highly sensitive dual-function sensor for refractive index and temperature using D-shaped microchannel photonic crystal fiber. Opt Express 32(7):12405–12418
34. Pravesh R, Kumar D, Pandey BP et al (2024) Design and analysis of a double D-shaped dual core PCF sensor for detecting biomolecules in the human body. IEEE Sens J 24(9):14159–14166
35. Walid A, Roy T, Hasan MM et al (2024) Design and performance analysis of a highly sensitive photonic crystal fiber based plasmonic sensor. Opt Quantum Electron 56(6):1042
36. Guo X, Sang T, Yang G et al (2024) Dual-polarization SPR sensor of U-shaped photonic crystal fiber coated with Au-TiO2. Plasmonics 20(5):2665–2674. https://doi.org/10.1007/s11468-024-02501-3
37. Zhang S, Wang Y (2024) A PCF-SPR sensor for dual-polarization and wide refractive index detection range. Opt Commun 569:130810